Effects of functional graft polymers on phase separation and ion-channel structures in anion exchange membranes analyzed by SANS partial scattering function

Kimio Yoshimura,[1] Akihiro Hiroki,[1] Aurel Radulescu,[2] Yohei Noda,[3] Satoshi Koizumi,[3]
Yue Zhao,[1,*] Yasunari Maekawa[1,*]

[1]*Department of Advanced Functional Materials Research, Takasaki Institute for Advanced Quantum Science, National Institutes for Quantum Science and Technology (QST), Watanuki-machi 1233, Takasaki, Gunma, 370-1292, Japan*
[2]*Forschungszentrum Jülich GmbH, Jülich Centre for Neutron Science @ MLZ, Lichtenbergstraße 1, D-85747 Garching, Germany*
[3]*Department of Engineering, Ibaraki University, Hitachi 316-8511, Japan*

*To whom all correspondence should be addressed: Yue Zhao (zhao.yue@qst.go.jp); Yasunari Maekawa (maekawa.yasunari@qst.go.jp)

Effects of functional graft polymers on phase separation and ion-channel structures in anion exchange membranes analyzed by SANS partial scattering function

Kimio Yoshimura, Akihiro Hiroki, Aurel Radulescu, Yohei Noda, Satoshi Koizumi, Yue Zhao, Yasunari Maekawa

for Table of Contents use only

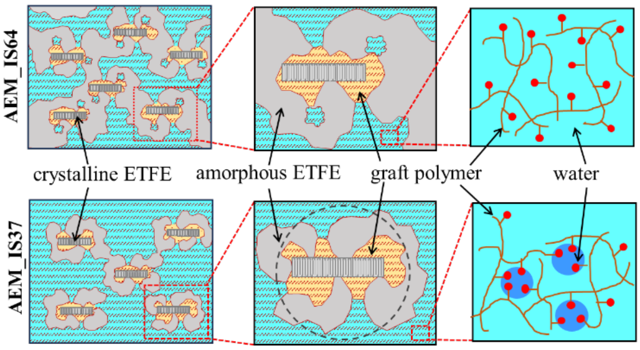

Abstract:

The partial scattering function (PSF) analysis through contrast variation small-angle neutron scattering experiments is applied to characterize structures of anion-exchange membranes (AEMs), prepared by graft copolymerization of 2-methyl-*N*-vinylimidazolium (Im) and styrene (St) monomers with Im/St ratios of 62/38 and 26/74 (denoted as AEM_IS64 and AEM_IS37, respectively), on a poly(ethylene-co-tetrafluoroethylene) base polymer (BP). The PSF self-terms can be expressed by the combination of mass fractal, Teubner-Strey, Guinier exponential, and Hard-sphere structural models to give exact structural information such as shape and size of individual domains of hydrophobic BP, hydrophilic graft-polymer (GP) and water (W). For AEM_IS64, the hydrophilic ion channels (GP/W domains) show bicontinuous and spherical structures with a mean separation distance of 33-34 nm and a radius of 4.0 nm, respectively. This result suggests a new structural feature of the coexistence of bicontinuous and isolated GP/W spheres. Furthermore, in a low *q*-region, slightly larger fractal dimension for GP (~1.7) than those of BP and W (~1.1) strongly supports the previously proposed “conducting and non-conducting two-phase structure” because only GP distributes in both phases. In AEM_IS37, GP/W and BP domains show an ion channel network structure with random particles having an average radius of gyration of 10.0 nm, and hard-sphere model fitting in the high-*q* region confirms previously proposed “water-puddle” structure with 3.8 nm diameter. PSF analysis in this work visualized the entire hierarchical structure of individual components in graft-type AEMs, providing mechanistic insights into the effects of functional GPs on phase-separation and ion channel structures.

I. Introduction

Anion exchange membranes (AEMs), as the "heart" of electrochemical cells such as fuel cells, redox flow batteries, electrolyzers, and water desalination, have attracted lots of attention for over a decade due to their low-cost and manufacturing feasibility in comparison with proton exchange membranes (PEMs).[1-6] AEMs are usually composed of polymers that are covalently bonded to different types of cations such as quaternary ammonium cations,[7-9] imidazoliums,[10-12] phosphoniums,[13, 14] and others[15] and are expected to efficiently transport ions from one side of the membrane to the other side without destroying either the ionic form or membrane texture and property. In general, the membrane properties must be carefully balanced to yield a satisfactory combination of ionic conductivity, chemical stability, and mechanical integrity under dynamic operation conditions.

To make a desired AEM, we have reported the radiation grafting technique in our previous studies, which may offer great advantages of low-cost fabrication and the adaptability of polymer synthesis and functionalization by optimizing the base polymer, graft monomers and grafting parameters.[16–19] Successful examples of radiation-grafted AEMs covered fluorinated polymer films such as polytetrafluoroethylene, poly(ethylene-*co*-tetrafluoroethylene) (ETFE), poly(vinylidene fluoride) or fully aromatic hydrocarbon polymers like poly(ether ether ketone).[10-25] Among them, we found ETFE-based imidazolium-type AEMs exhibited excellent balanced properties of lower water uptake (WU), higher conductivity, and higher alkaline stability than ammonium-type AEMs due to the low basicity as an Arrhenius base.[1-3, 26, 27] Particularly, the well-designed ETFE based AEMs by radiation graft copolymerization of 2-methyl-*N*-vinylimidazole (Im) that has methyl-protecting group at imidazole C-2 position and styrene (St) with an Im/St ratio of 6/4, were found to have good alkaline durability due to the effectively suppressed β-elimination and ring-opening hydrolysis.[12, 21]

The further systematic study of the effect of graft hydrophobicity on membrane structures, and their correlation to electrochemical properties and alkaline durability of the membrane was performed on these types of AEMs with the same ion-exchange capacity (IEC~ 1.0 mmol/g) but different Im/St ratios of 62/38, 38/62 and 26/74 (designated as AEM_IS64, AEM_IS46 and AEM_IS37, respectively). All AEMs show similar initial anion conductivity but a reverse relationship that low hydrophilicity resulted in low alkaline durability was found as reported in ref. 12. This unexpected phenomenon was interpreted by the hierarchical structures of AEMs.[12] Two structural characteristics were proposed in that work using the contrast variation small-angle neutron scattering (CV-SANS) method: (1) "conducting/nonconducting two-phase" model as illustrated in Scheme 1(a) was proposed to describe the microphase-separation structure in the length scale of >10 nm. It gave a first-time quantitative estimation of graft polymer distribution, which provides more precise structure details than "crystalline/amorphous two-phase" model used before.[21] This model revealed that the fractions of graft polymers in the conducting domains (presumed to be made of the conducting GP and water) for AEM_IS64, AEM_IS46 and AEM_IS37 are 0.52, 0.82 and 0.88, respectively.[12] It predicted the existence of water unreachable graft polymers embedded in the nonconducting (or hydrophobic) domains, particularly for AEM_IS64 with a low grafting degree (GD); (2) a hard-sphere fluid model was used to describe the local structure in ion channels of AEM_IS46 and AEM_IS37, which show nanophase-separated water puddles with a size of 3-4 nm, while AEM_IS64 shows homogenously dispersed ions without any evidenced local nanophase separation, as illustrated in Scheme

1(b). In AEM_IS46 and AEM_IS37, the imidazolium groups located at the boundary between graft polymers and water puddles were susceptible to hydrolysis, and hence, these two AEMs are less alkaline durable than AEM_IS64.

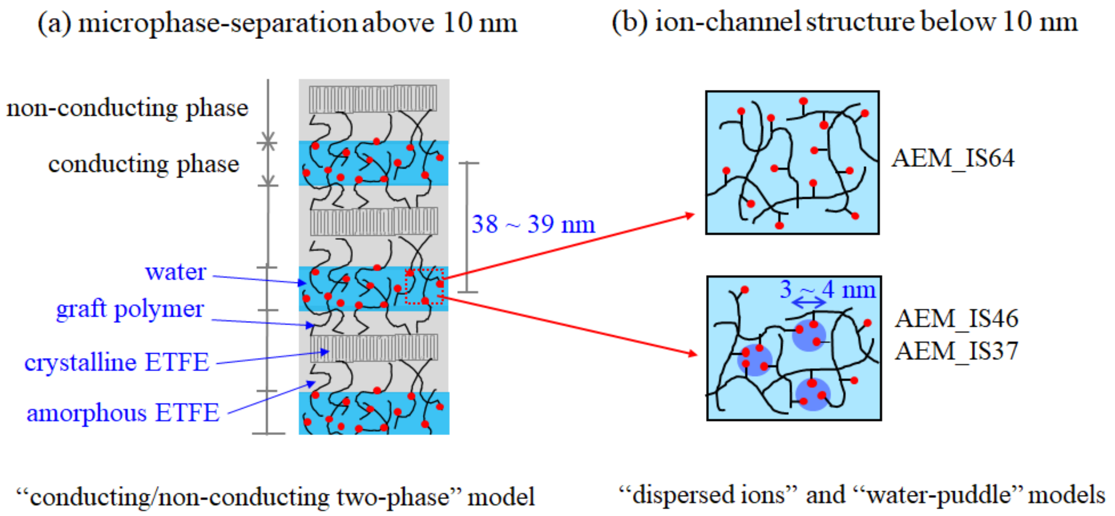
(a) microphase-separation above 10 nm
(b) ion-channel structure below 10 nm

“conducting/non-conducting two-phase” model
“dispersed ions” and “water-puddle” models

Scheme 1 Schematic illustrations of (a) “conducting/non-conducting two-phase” model to describe microphase-separation in AEMs above 10 nm; (b) “dispersed ions” and “water-puddle” models to describe ion-channel structures below 10 nm. (Adapted from Soft Matter 2018, 14, 9118-9131. Copyright [2018] Royal Society of Chemistry.)

The abovementioned structural model analysis gave a pioneering attempt on the understanding of graft-type AEMs’ structures in a quantitative manner. Note that in most of the graft-type PEMs and AEMs including the ETFE-based AEMs, many groups have confirmed that the functionalized graft domains acting as ion channels are mainly formed during the radiation-induced graft polymerization step.[21] The following ionization step to introduce ionic groups to graft polymer chains induces little change in correlation distances of lamellar stacks and crystallites.[21] Therefore, the structures of functionalized graft domain and the hydrophobic ETFE matrix in AEMs are kinetically determined after the graft polymerization. Upon hydration, the absorption of water by ionic groups will induce/enhance the hydrophilic/hydrophobic phase-separation between ion-channels and the hydrophobic base polymer matrix in the membrane, leading to more or less the hydrophilic polymer relaxation but not significant change in morphology or hierarchical structures of the graft-type AEMs. Accordingly, the morphology of the graft-type PEMs and AEMs is not in an equilibrated state, especially at a temperature lower than their glass transition temperature.

All the previous structural analysis was based on the scattering intensity profile $I(q)$, which was presumed to describe the typical structure pattern of a system without assigning components. Such analysis may give a possible structural pattern, while fail to identify the quantitative structure information of each component in the membrane such as ETFE base polymer, graft polymer, and water, and the structural correlations among different components. In addition, the previous work only analyzed the phase-separated structures in a limited length scale based on the assumption that the ion-channels contain two components of conducting GP and water, but it never reached a clear entire structural pattern with components' shape, size, spatial distribution and position from sub-nm to several hundred nm, the information on which is very crucial for the deep understanding of functional polymer effects on AEM properties.

The conventional measured $I(q)$ cannot individually provide the structure of hydrophobic polymer, hydrophilic polymer, ions, and water molecules, because it contains mixed structural information on all components. This undesirable original data problem is solved by partial scattering function (PSF) analysis through CV-SANS experiments.[28–32] PSF was recently developed by us to successfully elucidate the concrete hierarchical structure of the benchmark material Nafion and the well-studied radiation-grafted PEM, consisting of poly(styrene sulfonic acid) grafted onto ETFE base films (ETFE-g-PSSA).[30–32] Compared to the previously proposed structural models focusing on the pattern of scatters without component assignment, PSF analysis advances for the precise visualization and quantification of structures with the exact location of each component in the material. In this study, we applied the PSF analysis to elucidate the detailed hierarchical structure of each component in hydrated graft-type AEM_IS64 and AEM_IS37, representing two typical ion-channel structures shown in Scheme 1(b), in multiple length scales and to provide mechanistic insight into graft hydrophobicity and structure correlations. As PSF was for the first time used to characterize AEM structures, we would specify the typical and unique structures by comparing to PEMs such as Nafion and graft-type ETFE-g-PSSA.[30-32]

II. Experimental details

II-1. CV-SANS measurements

The detailed sample preparation and characterization of AEM_IS64 and AEM_IS37 can be found in our previous report and S1 in the supporting information.[12] The main characteristics of the two AEMs are listed in Table 1.

Table 1 Characteristics of AEM_IS64 and AEM_IS37 equilibrated in water at 25 °C.[1]

AEM_	Im/St	GD (%)	WU (%)	IEC (mmol g^{-1})	σ^2 (mS cm^{-1})	$\sigma_t/\sigma_0{}^3$	ϕ_{graft}	ϕ_{ETFE}	ϕ_w
IS64	62/38	30	15	0.95	58	40%	0.281	0.54	0.179
IS37	26/74	110	35	1.12	60	2%	0.447	0.246	0.307

[1] All data listed in Table 1 are referred from ref. 12.

[2] The conductivity of AEMs in OH^- form at 60 °C.

[3] The relative conductivity after AEMs were soaked in 1 M KOH at 80 °C for 200 h.

CV-SANS measurements were performed on KWS-2 SANS diffractometer operated by Juelich Centre for Neutron Science at the neutron source Heinz Maier-Leibnitz (FRM II reactor) in Garching, Germany.[33] All AEMs were measured in their bicarbonate (HCO_3^-) form to prevent degradation. The experimental details can be found in Ref. 12 and S1 in the supporting information. The $I(q)$ profiles at representative volume fraction of D_2O (f_{D2O}) in CV-SANS measurements were re-plotted in Figure S1 (symbols) in the supporting information, referred from the previous paper.[12]

II-2. Decomposition of scattering intensity profiles into partial scattering functions

Following the strategy that we applied to the hydrated Nafion and grafted PEM (ETFE-g-PSSA),[30-32] the hydrated AEM_IS64 and AEM_IS37 are partitioned into separate components of ETFE base polymer (BP), graft polymer (GP), and water as shown in Scheme 2.

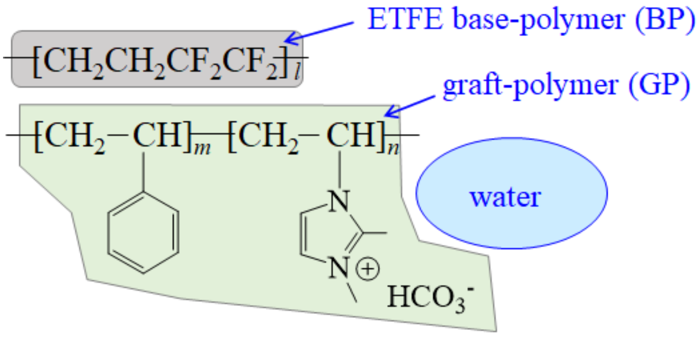

Scheme 2 An illustration of the three-component system of the hydrated AEMs composed of base polymer (BP), graft polymer (GP) and water (W) in AEM_IS64 (n:m = 62:38), and AEM_IS37 (n:m = 26:74).

It is worthy to show the mathematical foundation of the decomposition of $I(q)$ in CV-SANS experiments into PSFs, corresponding to the abovementioned components before the experimental results. We here omit the detailed description that can be found in the supporting information S2 and our previous work,[30-32] and only give the main equation on the basis of the incompressibility assumption that $I(q)$ is described using three PSF self-terms,

$$I(q) = (b_{BP} - b_{GP})(b_{BP} - b_W)S_{BP-BP}(q) + (b_{GP} - b_{BP})(b_{GP} - b_W)S_{GP-GP}(q) + (b_W - b_{BP})(b_W - b_{GP})S_{W-W}(q) \qquad (1)$$

where b_i and $S_{ii}(q)$ are the scattering length density (SLD) and PSF self-term of the i component (i = BP: base polymer, GP: graft polymer and W: water). S_{ii} is defined as

$$S_{ii}(q) = \frac{1}{V} < \iint \delta\varphi_i(\vec{\mathrm{r}})\delta\varphi_i\left(\vec{\mathrm{r}'}\right) \exp\left[-i\vec{q}\left(\vec{\mathrm{r}} - \vec{\mathrm{r}'}\right)\right] d\vec{\mathrm{r}}d\vec{\mathrm{r}'} > \qquad (2)$$

where V is the scattering volume and $\delta\varphi_i(\vec{\mathrm{r}})$ is the fluctuation part of the volume fraction of the i component ($\varphi_i(\vec{\mathrm{r}})$) at position $\vec{\mathrm{r}}$. $S_{ii}(q)$ represents the structure of the i component and is determined mathematically through CV-SANS technique as detailed in S2 and S3 in the supporting information.

The PSF cross-term S_{ij} ($i \neq j$), defined by the following equation,

$$S_{ij}(q) = \frac{1}{V} < \iint \delta\varphi_i(\vec{\mathrm{r}})\delta\varphi_j\left(\vec{\mathrm{r}'}\right) \exp\left[-i\vec{q}\left(\vec{\mathrm{r}} - \vec{\mathrm{r}'}\right)\right] d\vec{\mathrm{r}}d\vec{\mathrm{r}'} > \qquad (3)$$

can be deduced from S_{ii} using Eqs (4)–(6) under the incompressibility assumption.[30-32]

$$S_{BP-GP} = \frac{1}{2}(S_{W-W} - S_{BP-BP} - S_{GP-GP}) \qquad (4)$$

$$S_{GP-W} = \frac{1}{2}(S_{BP-BP} - S_{GP-GP} - S_{W-W}) \qquad (5)$$

$$S_{BP-W} = \frac{1}{2}(S_{GP-GP} - S_{BP-BP} - S_{W-W}) \qquad (6)$$

S_{ij} contains information about the interaction between the *i* and *j* components and their relative positions.

III. Results

III-1. Partial scattering function analysis

Self-terms. The SLD of each component was calculated using its chemical structure and mass density.[12, 36] Theoretically derived SLDs of BP (b_{BP}) and GP (b_{GP}) in both AEMs are listed in Table 2. Note that b_{GP} of these two AEMs are slightly higher than the reported values in the SI in ref. 12 because we take the counter ion HCO_3^- into account in this study. Water's SLD (b_W) varies as a function of f_{D2O}:

$$b_W = b_{D2O} f_{D2O} + b_{H2O}(1 - f_{D2O}) \qquad (7)$$

where b_{D2O} and b_{H2O} are the SLD of D_2O and H_2O being 6.34 and −0.56 (× 10^{10} cm^{-2}), respectively.[36]

Table 2 SLD (b_x) of each component in the hydrated AEM_IS64 and AEM_IS37.

b_x (×10^{10} cm^{-2})	BP	GP	Water
AEM_IS64	2.74	1.27	eq. (7)
AEM_IS37	2.74	1.35	eq. (7)

With these well-defined SLD values, the three PSF self-term S_{ii} for AEM_IS64 and AEM_37 are calculated using Eq. (1) as detailed in S3 in the supporting information and plotted as a function of *q* in Figures 1(a) and 1(b). All CV-SANS intensity profiles were reconstructed, as shown in Figures S1(a) and S1(b), using Eq (1) via back-substitution with these three PSF self-terms. The reconstructed *I*(*q*) profiles (solid lines) are well matched to the experimental profiles (symbols), indicating that S_{ii} with the appropriate SLDs is correct, *i.e.*, the PSF method is valid for these AEMs.

According to the scattering features of S_{ii}, we define three q-regions for classifying different structure hierarchies constructed by three components of BP, GP, and water: A small-q upturn in the low-q region at $q < 0.1$ nm^{-1} (Region I), a broad shoulder-like peak in the middle-q region at $0.1 < q < 0.9$ nm^{-1} (Region II), and the appearance of ionomer peak or not at $q > 0.9$ nm^{-1} (Region III).

For AEM_IS64, in Region I, S_{BP-BP} and S_{W-W} exhibit an upturn of power law relationship with the same power-law exponent (−1.1), while S_{GP-GP} gives a relatively larger power-law exponent (−1.7). In Region II, all S_{ii} show a shoulder-like scattering maximum with a center position at 0.17 nm^{-1}, which is close to the peak observed in the scattering intensity profiles in Figure S1(a). S_{GP-GP} shows a Porod's law tail following the peak, while S_{W-W} shows excess scattering at around $q \sim 0.5$ nm^{-1} and above before following the Porod's law tail at $q > 0.7$ nm^{-1}, which has never been observed in the previous analysis and will be discussed in section IV-2 in conjunction with structural model analysis. In Region III, all S_{ii} follow Porod's law, which was also noted in the $I(q)$ profiles in Figure S1(a).[12, 34]

For AEM_IS37, all S_{ii} exhibit an upturn with the same power-law exponent of −1.6 in Region I, and a broad shoulder-like scattering maximum in Region II. In Region III, they show clear peaks with a center position at ~1.29 nm^{-1}, which are close to the ionomer peak observed in the $I(q)$ profiles in Figure S1(b).

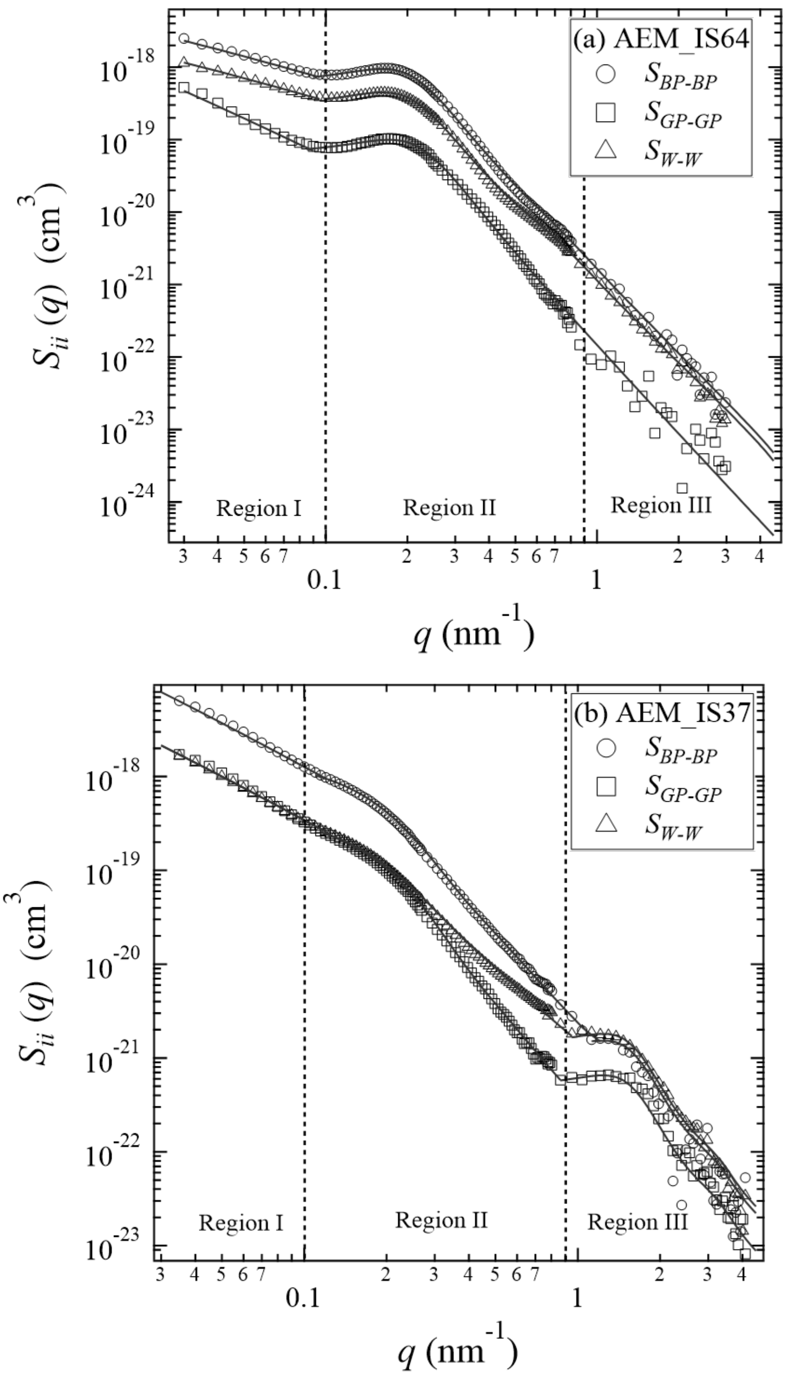

Figure 1 PSF self-terms (symbols) of the hydrated (a) AEM_IS64; and (b) AEM_IS37, and the best-fitted results (solid lines) by Eqs. (14) and (16) with the fitting parameters listed in Tables 3 and 4, respectively.

Cross-terms. The PSF cross-terms S_{ij} ($i \neq j$) that reflect cross-correlation between the components i and j are obtained through Eqs.(4)–(6), and plotted as a function of q

for AEM_IS64 and AEM_IS37 in Figures 2(a) and 2(b), respectively. The corresponding enlarged plots at high-q range are shown in Figures S2(a) and S2(b) in the supporting information. The sign of S_{ij} reveals the interaction force between i and j, with positive and negative values implying possibly attractive and repulsive interactions, respectively. For both AEMs, $S_{BP\text{–}GP}$ and $S_{BP\text{–}W}$ are negative, but $S_{GP\text{–}W}$ is positive at $q < 1.5$ nm^{-1}, thus the possible interactions between the pair components are repulsive and attractive, respectively. All S_{ij} is close to zero at $q > 1.5$ nm^{-1}, indicating a weak correlation among different components in a length scale < 4 nm, the phenomenon of which is different from our previously reported Nafion in which the side chain and water show clear positive correlations throughout the whole q-range including the high-q region.[30] Note that the analysis on SANS profiles of dry AEMs in ref. 12 shows that the phase-separation between BP and GP in these AEMs is strong, evidence by the Porod-law relationship (q^{-4}) in the high q-range at $q > 0.5$ nm^{-1}. This observation suggests that the graft polymerization proceeded in the amorphous ETFE phase results in the formation of clearly phase-separated conducting layers consisting of graft polymers, which were segregated from the ETFE substrate with a relevant sharp interface.[12]

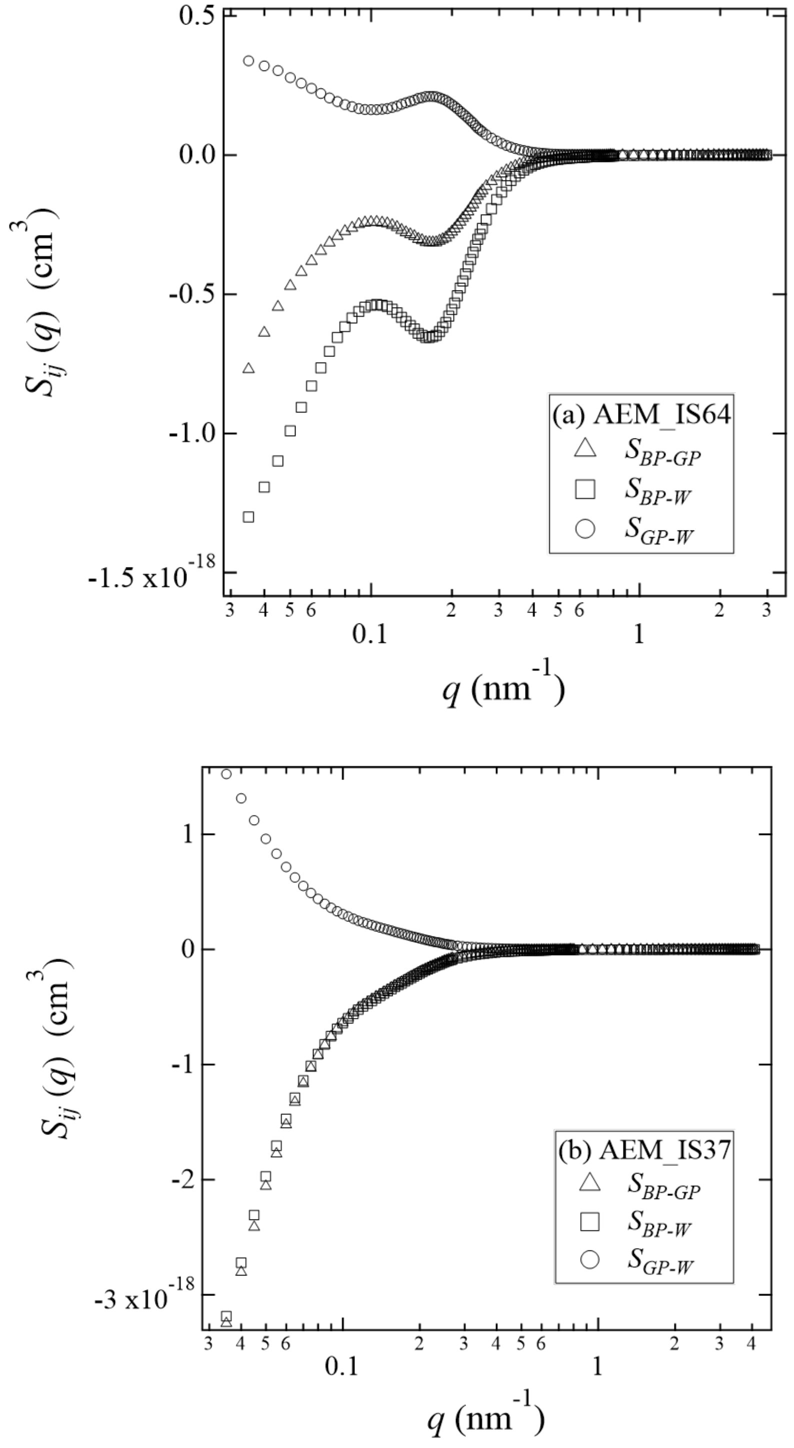

Figure 2 PSF cross-terms of the hydrated (a) AEM_IS64, and (b) AEM_IS37.

III-3. Fitting of S_{ii} using structural models

S_{ii} gives the concrete structure of the i component, including the arrangement and morphology of BP, GP, and water in AEMs. To interpret structure details of each component, a fitting function with three main terms corresponding to three q-Regions is applied to fit each S_{ii} profile of AEM_IS64 and AEM_IS37 as described below.

AEM_IS64. In Region I, all S_{ii} can be fitted well by mass fractal (MF) model because they show power-law dependence of q with an exponent < 3, which is a typical indicator of the mass fractal structure of self-assembly of phase-separated domains in small-angle scattering technique,[37, 38] expressed by

$$S_{MF}(q) \propto q^{-Df} \qquad (8)$$

where $S_{MF}(q)$ is the MF function with D_f being the fractal dimension. $S_{BP\text{–}BP}$ and $S_{W\text{–}W}$ have $D_f = 1.1$, while $S_{GP\text{–}GP}$ shows a larger value of $D_f = 1.7$.

In Region II, all S_{ii} show a clear scattering maximum at q around 0.17 nm^{-1}, and in particular, $S_{W\text{–}W}$ shows excess scattering maximum at $q \sim 0.5\ \mathrm{nm}^{-1}$. Thus, we construct a fitting function as the coexistence of two previously reported structural models: Teubner-Strey (TS) model and Hard-Sphere (HS) liquid model, as expressed below:[30, 31, 39-43]

$$S_{co}(q) \sim X_{TS} S_{TS}(q) + (1 - X_{TS}) S_{HS}(q) \qquad (9)$$

where

$$S_{TS}(q) \sim \frac{8\pi d^4}{\varepsilon[16\pi^4 + 8d^2\pi^2(\varepsilon^{-2} - q^2) + d^4(\varepsilon^{-2} + q^2)^2]} \qquad (10)$$

is the TS function that describes irregularly shaped bicontinuous domains with d being the mean distance between two domains determined from the peak position, q_m ($d = 2\pi/q_m$), and ε being considered as the dispersion of d (inversely proportional to the peak width). $S_{HS}(q)$ is HS model expressed below in eq. (11) that describes the structure composed of spherical particles with an average radius (R_s).[36, 41-43]

$$S_{HS}(q) \sim P(q) S(q) \qquad (11)$$

where $P(q)$ is the form factor of the spherical particles given by,

$$P(q) = v^2\{\frac{3[\sin(qR_s) - qR_s\cos(qR_s)]}{(qR_s)^3}\}^2 \qquad (12)$$

with v being the volume of the sphere. The Gaussian distribution function is applied to modify $P(q)$ with a size distribution as detailed in S4 in the supporting information. $S(q)$ is the interference factor for a random arrangement of spherical particles, given by Percus–Yevick approximation expressed as a function of the volume fraction of spheres (ϕ_s) and R_s.[41]

$$S(q\ ) = \frac{1}{1 + 24\phi_s(\frac{F(A)}{A})} \qquad (13)$$

where $A = 2qR_s$ and $F(A)$ is a trigonometric function of A as detailed in Ref. 12 and S4 in the supporting information.

X_{TS} is the relative fraction of $S_{TS}(q)$ in the fitting of two models in eq. (9). $S_{GP–GP}$ that has no excess scattering can be well fitted by eq (9) with $X_{TS} = 1.0$. While for $S_{W–W}$ and $S_{BP–BP}$, the best fitting is achieved by setting a proper X_{TS} in eq. (9).

In Region III, all S_{ii} show the typical Porod law relationship of $S_{Porod}(q) \sim q^{-4}$, representing the smooth interface among domains at high-q regime.[34]

Thus, the final fitting function is written as the sum of the three models:

$$S_{ii}(q) = C_1S_{MF}(q) + C_2S_{co}(q) + C_3S_{Porod}(q) + C_B \qquad (14)$$

where C_1, C_2, and C_3 are the fitting constants, and C_B is the constant background.

The best-fitted curves obtained using Eq. (14) are shown together with S_{ii} in Figure 1(a), and the fitting parameters are listed in Table 3.

AEM_IS37. As shown in Figure 1(b), in Region I, similar to AEM_IS64, all S_{ii} can be well fitted by MF model with $D_f = 1.6$. In Region II, since the abovementioned fitting function in eq. (9) did not provide an adequate fit to the data, we decided to follow our previous fitting rules for grafted PEMs, ETFE-g-PSSA, that the immiscibility between GP and BP drives individual GP domains being randomly formed during the graft polymerization in the irregular shape, which can be well fitted by the unified Guinier-exponential function (GE model). Therefore, here we employ GE model function, $S_{GE}(q)$, to fit S_{ii} in Region II, which is in an approximate form of a Guinier's law and a power-law as expressed below,[31, 44-46]

$$S_{GE}(q) \propto \exp\left(\frac{-q^2 {R_g}^2}{3}\right) + B\left\{\frac{[\mathrm{erf}\left(\frac{kqR_g}{\sqrt{6}}\right)]^3}{q}\right\}^P \qquad (15)$$

where R_g is the radius of gyration of the irregularly shaped particle, erf(x) is the error function of x, and k is an empirical constant ~1.06, and B is a constant pre-factor. P is the power law component, indicating the particle's surface fractal dimension if $3 < P < 4$, or a mass fractal dimension of the sub-structure level if $P < 3$. In Region III, we again choose our previously proposed HS fluid model in Ref. 12 and eq. (11) to describe the local structure in ion channels.

Thus, the final fitting function for AEM_IS37 is written as the sum of the abovementioned three models:

$$S_{ii}(q) = C_1{}'S_{MF}(q) + C_2{}'S_{GE}(q) + C_3{}'S_{HS}(q) + C_B{}' \qquad (16)$$

Where $C_1{}'$, $C_2{}'$, and $C_3{}'$ are the fitting constants, and $C_B{}'$ is the constant background.

The best-fitted curves obtained using Eq. (16) are shown together with S_{ii} in Figure 1(b) and the fitting parameters are listed in Table 4.

Table 3 Structural models for PSF self-terms in each q-region with best-fitting parameters in Eq (14) for AEM_IS64

q-Region	Region I:	Region II:

Models	MF model	TS model (bicontinuous)			HS model (sphere)	
S_{ii}	D_f	X_{TS}	d (nm)	ε (nm)	R_s (nm)	ϕ_s
S_{BP-BP}	1.10±0.05	0.85±0.05	33.5±0.5	10.5±0.2	4.0±0.2	0.075±0.005
S_{GP-GP}	1.70±0.05	1.0	32.5±0.5	10.5±0.2	-	-
S_{W-W}	1.10±0.05	0.60±0.05	34.0±0.5	11.2±0.2	4.0±0.2	0.075±0.005

Table 4 Structural models for PSF self-terms in each q-region with best-fitting parameters in Eq (16) for AEM_IS37

q-Region	Region I:	Region II:		Region III:	
Models	MF model	GE model (random particle)		HS model (sphere)	
S_{ii}	D_f	R_g (nm)	P	R_s (nm)	ϕ_s
S_{BP-BP}	1.60±0.05	10.2±0.2	3.30±0.05	1.90±0.05	0.20±0.01
S_{GP-GP}	1.60±0.05	10.2±0.2	3.60±0.05	1.90±0.05	0.20±0.01
S_{W-W}	1.60±0.05	10.2±0.2	3.10±0.05	1.90±0.05	0.20±0.01

IV. Discussion

IV-1. CV-SANS results

According to Babinet's principle that states the diffraction pattern from an opaque body being identical to that from a hole of the same size and shape,[30, 35] if the system is composed of only two components, CV-SANS experiments will change the absolute intensity but not the shape of the profile. Therefore, these hydrated AEMs are not a simple "two-component" system (see Figures S1(a) and S1(b) in the supporting information), which suggests us to use a more accurate "three-component" model as shown in Scheme 2, to explore the exact structure.

IV-2. Hierarchical structures of AEM_IS64: in comparison to grafted PEMs.

Region I ($q < 0.1$ nm^{-1}). MF structures are observed in only grafted membranes such as ETFE-g-PSSA and the current AEM_IS64, but not in the neat ETFE base film,[20, 21] therefore, the origin of the MF structures must be the aggregation of the small GP domains generated by the graft polymerization, which are incorporated into but clearly phase-separate from the BP matrix. The phase separated structures were evidenced by the repulsive interaction between GP and BP with the negative PSF cross term, $S_{BP\text{–}GP}$. Accordingly, the incorporation of GP domains makes the BP matrix deform into MF structure. In addition, the positive $S_{GP\text{–}W}$ and negative $S_{BP\text{–}W}$ indicate that water is closely attached to GP due to the strong interaction with ionic groups, but tends to depart away from BP. Thus, we conclude that water must have coordinative movement with GP to form GP/W domains that phase-separate from the BP matrix. This is the direct experimental evidence that strongly supports the assumption in our previous work that the conducting phase,[12] or hydrophilic ion channels,[21] are constructed by GP and water together, which are clearly phase-separated from non-conducting phase as shown in Scheme 1(a).

Fractal dimension, D_f, which is new information from the previous results, gives us more detailed information of the shapes and distribution of hydrophobic BP matrix and hydrophilic GP/W domains (ion channels). It indicates how effectively the structure fills the available space. Smaller and larger values of D_f imply a more and less compact packing density of the objects in the space, respectively. When particles self-assemble in terms of the dimension in the sense of 1-D, it gives $D_f = 1$. $S_{BP\text{–}BP}$ and $S_{W\text{–}W}$ show MF structure with a dimension of $D_f = 1.1$, quite close to 1-D objects such as rods, worms or tubes, which were not characterized in the previous papers.[12, 21] Therefore, it indicates that the ion channels have tube-like structure, which are often proposed in Nafion and aromatic hydrocarbon PEMs. The MF analysis on $S_{GP\text{–}GP}$ gives $D_f = 1.7$, larger than that of $S_{BP\text{–}BP}$ and $S_{W\text{–}W}$. The larger D_f for GP indicates more connections and branch-like structure of GP domains. This result is another strong proof supporting our previous characterization of "conducting/nonconducting two-phase" structure of AEM_IS64, where the GP was found to distribute in conducting and nonconducting phases with fractions of 52% and 48%, respectively. Namely, the conducting phase is constructed by homogeneously miscible water and GP and the nonconducting phase contains water-unreachable "dry" GP chains embedded in the BP matrix. Thus, the larger D_f for GP domains can be explained by the fact that the existence of the "dry" GP domains act as connections or branches of GP/W tube-like domains, both contributing to MF dimension of GP domains. The schematic picture of AEM_IS64 in Region I is shown in Figure 3 (a).

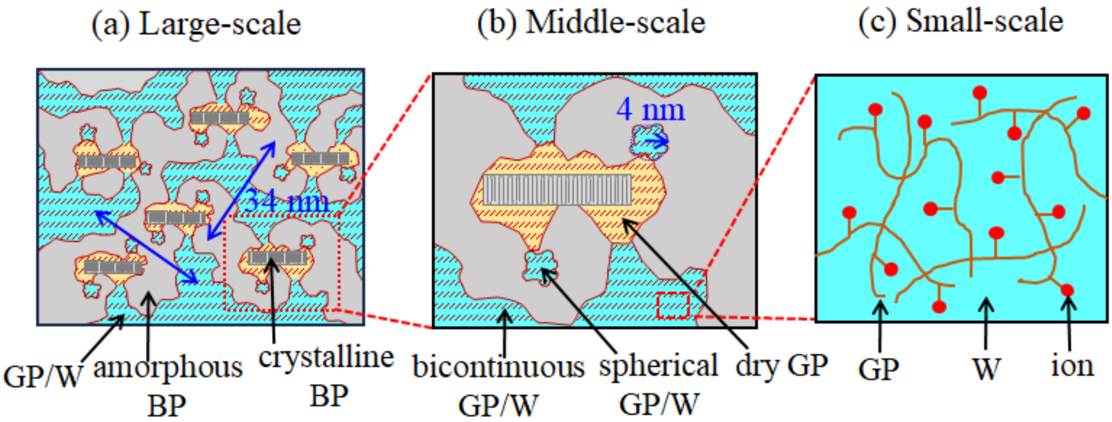

Figure 3 Schematic of the hierarchical structure of BP, GP, and water domains in the hydrated AEM_IS64 at (a) large-scale; (b) middle-scale; and (c) small-scale.

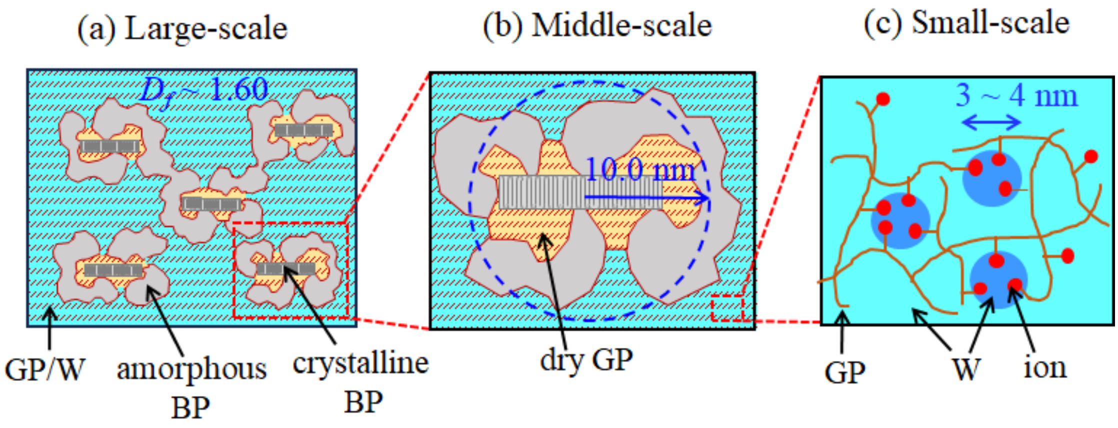

Figure 4 Schematic of the hierarchical structure of BP, GP, and water domains in the hydrated AEM_IS37 at (a) large-scale; (b) middle-scale; and (c) small-scale.

Region II (0.1 nm^{-1} < q < 0.9 nm^{-1}). Similar to Nafion but unlike ETFE-g-PSSA, all S_{ii} of AEM_IS64 show an obvious scattering maximum in Region II, suggesting that TS and HS models may work better than GE model for scattering profile fitting because a scattering maximum never appears in GE model. $S_{GP\text{-}GP}$ can be fitted well by TS model, indicating a typical bicontinuous-like structure with a mean separation distance d of 32.5 nm. Since $S_{W\text{-}W}$ exhibits excess scattering at around $q \sim 0.5$ nm^{-1} and above together with the typical scattering maximum, as mentioned in section III-1, it is best-fitted by a combination of TS and HS models in eq (9) with X_{TS} being 0.6. These fitting results indicate that 60% of water domains show the bicontinuous-like structure with similar d of 34 nm, and 40% (=1-X_{TS}) of them are more like discontinuous spherical particles with an average radius of 4.0 nm. Since GP and water domains are closely attached, judging from the positive $S_{GP\text{-}W}$ in this region and its similar peak shape and position to both $S_{GP\text{-}GP}$ and $S_{W\text{-}W}$, it can be concluded that all these water domains, no matter being bicontinuous or spherical shape, must be coexistent with GP to form hydrophilic GP/W domains. In other words, GP chains distribute in "dry" GP domains as well as in the "wet"

GP/W domains, being reflected by $S_{GP\text{-}GP}$, while water distributes only in “wet” GP/W domains, being reflected by $S_{W\text{-}W}$. When “dry” and “wet” GP domains are connected, they are treated as one domain in $S_{GP\text{-}GP}$. This explained why discontinuous GP spherical domains are not observed in $S_{GP\text{-}GP}$. According to the above analysis, the schematic picture of GP and water domains are drawn in Figure 3(b), which cannot be revealed without using structural model analysis based on PSF profiles in this study.

Note that the volume fraction of water in spherical domains ($\phi_{S,cal}$) can be theoretically calculated to be 0.072 in terms of X_{TS} and the total water fraction (ϕ_{W}) in the membrane, using the following equation, $\phi_{S,cal} = (1 - X_{TS})\phi_w$. This value is in good agreement with the fitting sphere volume fraction (ϕ_{S}) of 0.075 (Table 3), which was obtained independently using eq. (12), further confirmed the validity of TS-HS fitting function in eq. (9). The incorporation of GP/W domains in the BP matrix adds TS and HS structure patterns to the BP matrix, resulting in similar structural features in $S_{BP\text{–}BP}$ with a best-fitted X_{TS} being 0.85 as shown in Table 3.

It is generally believed that GP chains are randomly polymerized from the BP crystalline/amorphous interface and propagate in the BP amorphous phase during the radiation graft polymerization, as described in literature[47] and section S1.3 in the supporting information. It is also well-known crystalline (or oriented) polymers can act as a physical crosslink points. Thus, the BP crystallites most likely work as physical crosslink points of GPs, the closer to BP crystallites, the more density and constraints GPs have. According to the Flory-Rehner theory, the solvent swelling behavior of a network system is determined by the crosslink content, as well as interactions between polymer and absorbed molecules.[48] This theory is applicable to our AEMs to explain thermodynamically the reason why GP domains close to BP crystallites are swelling weaker than GP domains in BP inner amorphous domains, which results in the fact that only partially GPs can be ionized, and dry GP domains are formed around BP crystallites. GP domains in BP amorphous phase are isolated at the early stage, then they are gradually connected and fused to each other when the polymerization is going on.[30, 49] The total volume fraction of GP and W domains (0.46) in AEM_IS64, as shown in Table 1, implies the rational formation of bicontinuous-like ion channels. However, the volume fraction of GP (ϕ_{graft} ~0.281) is only a half of ETFE (ϕ_{ETFE} ~0.54), indicating a relatively early polymerization stage, at which there still exist isolated GP/W particles that cannot expand themselves enough to connect to one another to form bicontinuous ion-channels. These isolated GP/W particles tend to be more or less spherical in shape to minimize the interfacial free energy.

In addition to the previous characterization for the morphology of GP/W coordinative domains, representing exactly the conducting-phase that is defined in ref. 12, the PSF analysis in this work evidences the existence of "dry" GP domains by the fact that GP and water domains can be fitted by the different structural models, i.e., a TS-model for GP domains and the combination of TS- and HS- models for water domains, respectively. The existence of the spherical GP/W coordinative domains and "dry" GP domains result in a less-continuous conducting phase in AEM_IS64 and reduced ion transport efficiency compared to the continuous hydrophilic phase being bicontinuous-like domains in Nafion or network structure in ETFE-g-PSSA.

Region III (q > 0.9 nm^{-1}). All S_{ii} follow Porod law in Region III, meaning that GP and water are homogeneously distributed in ion-channels without evidence of local phase separation. Since this conclusion supports our previously proposed ion-channel structure shown in Scheme 1(b), the same schematic picture is employed as the exact local structure in Figure 3 (c).[12]

IV-2. Hierarchical structures of AEM_IS37: The Effect of graft polymer hydrophobicity on hydrophilic domains

Region I (q < 0.1 nm^{-1}). MF model analysis works well on all S_{ii} for AEM_IS37, as the case of abovementioned AEM_IS64 because of the same origin of the microphase-separation between GP and BP. However, different from the tube-like ion channels in AEM_IS64, all components in AEM_IS37 show similar MF structure with a dimension of $D_f = 1.6$, indicating all domains form connected network structures. Since BP and the coordinative GP/W domains are minor and major components in AEM_IS37 (ϕ_{ETFE} ~ 0.246), as shown in Table 1, we may reasonably conclude that it is the aggregates of the BP particles disperse in the GP/W matrix. The schematic picture of AEM_IS37 in Region I is shown in Figure 4 (a).

Note that a relatively smaller D_f of both AEM_IS64 and AEM_IS37 than that of previously reported ETFE-g-PSSA ($D_f = 2.4$)[32] indicates less compact packing density in ETFE based AEMs probably because the phase separation tendency between ETFE and Im-St copolymers is weaker than that between ETFE and PSSA. The different separation tendency should originate from the fact that Im-St copolymer has weak base (Im) with hydrophobic comonomer unit (St) while PSSA has strong acid group without hydrophobic comonomer unit. This drives a less clear phase separation and rough interface in AEMs than that in ETFE-PSSA, resulting in less compact packing, which is generated during the polymerization process.

Region II (0.1 nm^{-1} < q < 0.9 nm^{-1}). Unlike AEM_IS64, neither TS model nor TS-HS combined model could fit S_{ii} well for AEM_IS37, probably because the volume fraction of ETFE (ϕ_{ETFE} ~0.246) is much lower than the representative value at around 0.5, consisting of similar volume fractions of two phases, for bicontinuous-like structure. Therefore, we chose the GE model that was previously used in fitting ETFE-g-PSSA, to describe the irregularly shaped BP particles in Region II. The analysis shows the individual BP domain has a R_g of 10.0 nm, which is the average size of the individual BP building blocks to form the BP aggregates in Region I. The GP/W coordinative domains can be treated as one matrix phase, in which BP particles disperse and exhibit the same structural pattern as BP domains do according to the Babinet's principle.[35] Note that the cross-terms of $S_{BP\text{-}GP}$ and $S_{BP\text{-}W}$ are quite close to each other especially at $q < 0.3$ nm^{-1}, indicating that the structure of GP and W domains are similar in AEM_IS37, in that they coordinatively form GP/W domains together, and there exist nearly no separated GP or W domains outside of GP/W domains. This result is quite different from the case of AEM_IS64, where the amplitude of $S_{BP\text{-}GP}$ is obviously different from that of $S_{BP\text{-}W}$, possibly relating to the fact that dry GP domains exist as we discussed in section IV-1, which are separate from GP/W domains.

The power-law relationship in the high-q-regime in Region II allows for the estimation of P, which is 3.1~3.6 for all components. The smaller P value than the typical sharp Porod surface ($P = 4$) indicates the surface of BP particles is not smooth. Based on the above discussion, a schematic of the structure in Region II is shown in Figure 4(b).

Region III (q > 0.9 nm^{-1}). We applied the same HS-fluid model as reported before to fit S_{ii}.[12] The fitting of all S_{ii} gives $R_s = 1.9$ nm and $\phi_s = 0.20$, which are in good agreement with the previous analysis on the intensity profiles in that "water-puddles" distribute in the conducting (GP/W) domains.[12] The PSF analysis in this work confirms the previously proposed "water-puddles" structure as shown in Scheme 1(b). Accordingly, the same schematic structure is reprinted for Region III in Figure 4 (c).

As mentioned in the Introduction section, the imidazolium groups located at the boundary between graft polymers and water puddles in AEM_IS37 were susceptible to hydrolysis, and hence the AEM_IS37 is less alkaline durable than AEM_IS64. On the other hand, the water puddle has less influence on the conductivity, probably because it is located inside ion-channels. Even though AEM_IS46 and AEM_IS37 are expressed by different structures of bicontinuous and random particles, constructed by ion channels and hydrophobic BP matrix in Region II, respectively, the connectivity of ion channels is not much different, leading to similar conductivity to each other due to the same content of ionic groups (*i.e.*, IEC).

V. Conclusions.

We applied PSF analysis to hydrated radiation-grafted AEMs with different GP compositions through CV-SANS experiments to characterize more detailed structure of each component in the membrane, which plays the essential role for the required properties. The entire structural patterns of AEM_IS64 and AEM_IS37 were constructed in Figures 3 and 4, respectively. For AEM_IS64, the hydrophilic ion channels made of GP/W domains have bicontinuous and spherical structures with a mean separation distance of 33-34 nm and with a radius of 4.0 nm, respectively. GP domains show a larger low-q fractal dimension (~1.7) than those of BP and W (~1.1), which strongly supports the previously proposed conducting and non-conducting two-phase structure. In AEM_IS37, BP domains form a mass fractal network structure in the GP/W matrix, with particles having an R_g of 10.0 nm. Moreover, HS model fitting in high-q region confirms previously proposed water-puddle structures with 3.8 nm diameter, which again convinced the previous conclusion that the increase in the hydrophobicity of graft polymers in this type of AEMs is one crucial molecular design to generate nanophase separated water-rich puddles in ion channels in that accelerating alkaline degradation.

It should be mentioned again that individual structure of main components (BP, GP, and water) can be derived only by PSF analysis. This study certifies the unique capability of PSF analysis over the conventional intensity analysis to provide quantitative multiple length scale understanding in the effects of functional graft polymers on phase separation and ion-channel structures in AEMs. Beyond, it reveals the spherical structures consisting of GP and water in Region II in AEM_IS64, probably assigned to the hydrophilic terminal that cannot be connected to ion-channels. This in turn can help in the design of high-performing AEMs for a wide range of energy conversion applications.

Notes

The authors declare no competing financial interest.

Acknowledgments

This work was partially supported by Grant-in-Aid for Scientific Research (A) from Japan Society for the Promotion of Science (JSPS) (KAKENHI Grant Number: 18H03850), and partially supported by "Advanced functional polymer materials alliance" project under QST innovation hub program in collaboration with participant companies.

Supporting information

Preparation and characterization of radiation-grafted AEMs; Incompressibility assumption for a ternary system; Decomposition of scattering intensity profiles into partial scattering functions by contrast variation SANS; Hard-Sphere fluid model analysis; Experimental scattering intensity profiles (symbols) and the reconstructed intensity profiles (solid lines) of the hydrated (a) AEM_IS64; and (b) AEM_IS37, equilibrated in water mixtures of D_2O and H_2O with different ratios; Enlarged PSF cross-terms of the hydrated (a) AEM_IS64, and (b) AEM_IS37

References.

1. Varcoe, J. R.; Slade, R. C. T. Prospects for alkaline anion-exchange membranes in low temperature fuel cells, *Fuel Cells* **2005**, *5*, 187-200.
2. Si, Z.; Qiu, L.; Dong, H.; Gu, F.; Li, Y.; Yan, F. Effects of substitutes and substitution positions in alkaline stability of imidazolium cations and their corresponding anion-exchange membranes, *ACS Appl. Mater. Interfaces* **2014**, *6*, 4346-4355.
3. Varcoe, J. R.; Atanassov, P.; Dekel, D. R.; Herring, A. M.; Hickner, M. A.; Kohl, P. A.; Kucernak, A. R.; Mustain, W. E.; Nijmeijer, K.; Scott, K.; Xu, T.; Zhuang, L. Anion-exchange membranes in electrochemical energy systems, *Energy Environ. Sci.* **2014**, *7*, 3135-3191.
4. Couture, G.; Alaaeddine, A.; Boschet, F.; Ameduri, B. Polymeric materials as anion-exchange membranes for alkaline fuel cells, *Prog. Polym. Sci.* **2011**, *36*, 1521-1557.
5. Merle, G.; Wessling, M.; Nijmeijer, K. Anion exchange membranes for alkaline fuel cells: A review, *J. Membr. Sci.* **2011**, *377*, 1-35.
6. Wang, Y. J.; Qiao, J.; Baker, R.; Zhang, J. Alkaline polymer electrolyte membranes for fuel cell applications, *Chem. Soc. Rev.* **2013**, *42*, 5768-5787.
7. Hugar, K. M.; You, W.; Coates, G. W. Protocol for the quantitative assessment of organic cation stability for polymer electrolytes, *ACS Energy Lett.* **2019**, *4*, 1681−1686.
8. You, W.; Hugar, K. M.; Selhorst, R. C.; Treichel, M.; Peltier, C. R.; Noonan, K. J. T.; Coates, G. W. Degradation of organic cations under alkaline conditions, *J. Org. Chem.* **2021**, *86*, 254−263.
9. Marino, M. G.; Kreuer, K. D. Alkaline stability of quaternary ammonium cations for alkaline fuel cell membranes and ionic liquids, *ChemSusChem* **2015**, *8*, 513−523.

10. Yang, C.; Wang, S.; Ma, W.; Jiang, L.; Sun, G. Comparison of Alkaline Stability of Quaternary Ammonium- and 1,2-Methylimidazolium-based Alkaline Anion Exchange Membranes, *J. Membr. Sci.* **2015**, *487*, 12−18.

11. Zhao, Y.; Yoshimura, K.; Mahmoud, A. M. A.; Yu, H.-C.; Okushima, S.; Hiroki, A.; Kishiyama, Y.; Shishitani, H.; Yamaguchi, S.; Tanaka, H.; Noda, Y.; Koizumi, S.; Radulescu, A.; Maekawa, Y. A long side chain imidazolium-based graft-type anion-exchange membrane: novel electrolyte and alkaline-durable properties and structural elucidation using SANS contrast variation, *Soft Matter* **2020**, *16*, 8128−8143.

12. Yoshimura, K.; Zhao, Y.; Hiroki, A.; Kishiyama, Y.; Shishitani, H.; Yamaguchi, S.; Tanaka, H.; Koizumi, S.; Houston, J.; Radulescu, A.; Appavou, M.-S.; Richter, D.; Maekawa, Y. Reverse relationships of water uptake and alkaline durability with hydrophilicity of imidazolium-based grafted anion-exchange membranes, *Soft Matter* **2018**, *14*, 9118−9131.

13. Zhang, B.; Kaspar, R. B.; Gu, S.; Wang, J.; Zhuang, Z.; Yan, Y. A new alkali-stable phosphonium cation based on fundamental understanding of degradation mechanisms, *ChemSusChem* **2016**, *9*, 2374−2379.

14. Zhang, B.; Long, H.; Kaspar, R. B.; Wang, J.; Gu, S.; Zhuang, Z.; Pivovar, B.; Yan, Y. Relating alkaline stability to the structure of quaternary phosphonium cations, *RSC Adv.* **2018**, *8*, 26640−26645.

15. Pham, T. H.; Olsson, J. S.; Jannasch, P. Effects of the N-alicyclic cation and backbone structures on the performance of poly(terphenyl)-based hydroxide exchange membranes, *J. Mater. Chem. A* **2019**, *7*, 15895−15906.

16. Nasef, M. M. Radiation-grafted membranes for polymer electrolyte fuel cells: current trend and future directions, *Chem. Rev.* **2014**, *114*, 12278-12329.

17. Nasef, M. M.; Gürsel, S. A.; Karabelli, D.; Güven, O. Radiation-grafted materials for energy conversion and energy storage applications, *Progr. Polym. Sci.* **2016**, *63*, 1-41.
18. Nasef, M. M.; Güven, O. Radiation-grafted copolymers for separation and purification purposes: Status, challenges and future directions, *Progr. Polym. Sci.* **2012**, *37*, 1597-1656.
19. Gubler, L. Polymer design strategies for radiation-grafted fuel cell membranes, *Adv. Energy Mater.* **2014**, *4*, 1300827.
20. Tap, T. D.; Sawada, S.; Hasegawa, S.; Yoshimura, K.; Oba, Y.; Ohnuma, M.; Katsumura, Y.; Maekawa, Y. Hierarchical structure-property relationships in graft-type fluorinated polymer electrolyte membranes using small- and ultrasmall-angle X-ray scattering analysis, *Macromolecules* **2014**, *47*, 2373-2383.
21. Zhao, Y.; Yoshimura, K.; Shishitani, H.; Yamaguchi, S.; Tanaka, H.; Koizumi, S.; Szekely, N.; Radulescu, A.; Richter, D.; Maekawa, Y. Imidazolium-based anion exchange membranes for alkaline anion fuel cells: elucidation of the morphology and the interplay between morphology and properties, *Soft Matter* **2016**, *12*, 1567-1578
22. Iwase, H.; Sawada, S.; Yamaki, T.; Koizumi, S.; Ohnuma, M.; Maekawa, Y. Hierarchical structure analysis of graft-type polymer electrolyte membranes consisting of cross-linked polytetrafluoroethylene by small-angle scattering in a wide-q range, *Macromolecules* **2012**, *45*, 9121-9127.
23. Mortensen, K.; Gasser, U.; Guersel, S. A.; Scherer, G. G. Structureal characterization of radiation-grafted block copolymer films using SANS technique, *J. Polym Sci. Polym. Phys. Ed.* **2008**, *46*, 1660-1668.

24. Chen, J.; Asano, M.; Maekawa, Y.; Yoshida, M. Suitability of some fluoropolymers used as base films for preparation of polymer electrolyte fuel cell membranes, *J. Membr. Sci.* **2006**, *277*, 249-257.
25. Hasegawa, S.; Sato, K.; Narita, T.; Suzuki, Y.; Takahashi, S.; Morishita, N.; Maekawa, Y. Radiation-induced graft polymerization of styrene into a poly(ether ether ketone) film for preparation of polymer electrolyte membranes, *J. Membr. Sci.* **2009**, *345*, 74-80.
26. Yoshimura, K.; Koshikawa, H.; Yamaki, T.; Shishitani, H.; Yamamoto, K.; Yamaguchi, S.; Tanaka, H.; Maekawa, Y. Imidazolium cation based anion-conducting electrolyte membranes prepared by radiation induced grafting for direct hydrazine hydrate fuel cells, *J. Electrochem. Soc.*, **2014**, *161*, F889-F893.
27. Koshikawa, H.; Yoshimura, K.; Sinnananchi, W.; Yamaki, T.; Asano, M.; Yamamoto, K.; Yamaguchi, S.; Tanaka, H.; Maekawa, Y. Counter-anion effect on the properties of anion-conducting polymer electrolyte membranes prepared by radiation-induced graft polymerization, *Macromol. Chem. Phys.* **2013**, *214*, 1756-1762.
28. Shibayama, M. Chapter 8 Soft Condensed Matter, *Experimental Methods in the Physical Sciences, Neutron Scattering-applications in biology, chemistry and materials science,* edited by Fernandez-Alonso, F. and Price D. L., **2017**, *46*, 459-546.
29. Endo, H.; Schwahn, D.; Colfen, H. On the role of block copolymer additives for calcium carbonate crystallization: small angle neutron scattering investigation by applying contrast variation, *J. Chem. Phys.* **2004**, *120*, 9410-9423.
30. Zhao, Y.; Yoshimura, K.; Motegi, T.; Hiroki, A.; Radulescu, A.; Maekawa, Y. Three-component domains in the fully hydrated Nafion membrane characterized by partial scattering function analysis, *Macromolecules* **2021**, *54*, 4128-4135.

31. Zhao, Y.; Yoshimura, K.; Sawada, S.; Motegi, T.; Hiroki, A.; Radulescu, A.; Maekawa, Y. Unique structural characteristics of graft-type proton exchange membranes uusing SANS partial scattering function analysis, *Macromolecules* **2022**, *55*, 7100-7109.
32. Zhao, Y.; Yoshimura, K.; Sawada, S.; Hiroki, A.; Radulescu, A.; Maekawa, Y. Macroscopic determination of the local hydration number of polymer electrolyte membranes using SANS partial scattering function analysis, *ACS Macro Lett.* **2023**, *12*, 481-486.
33. Radulescu, A.; Pipich, V.; Frielinghaus, H.; Appavou, M. S. KWS-2, the high intensity / wide Q -range smallangle neutron diffractometer for soft-matter and biology at FRM II, *Journal of Physics: Conference Series* **2012**, *351*, 012026.
34. Porod, G. Die Röntgenkleinwinkelstreuung von dichtgepackten kolloiden Systemen, *Kolloid Zeit* **1951**, *124*, 83-114.
35. Born, M.; Wolf, E. *Principles of Optics*; Cambridge University Press: Cambridge, 1999.
36. See for example, Roe, R. J. *Methods of X-ray and neutron scattering in polymer science*; Oxford Uni. Press: New York, 2000.
37. Sinha, S. K.; Freltoft, T.; Kjems, J. in *Kinetics of Aggregation and Gelation*; Family, F.; Landau D. P. Eds.; Elsevier: Amsterdam, 1984.
38. Freltoft, T.; Kjems, J.; Sinha, S. K. Power-law correlations and finite-size effects in silica particle aggregates studied by small-angle neutron scattering, *Phys. Rev. B* **1986**, *33*, 269-275.
39. Balog, S.; Gasser, U.; Mortensen, K.; Ben youcef, H.; Gubler, L.; Scherer, G. G. Nano-scale morphology in graft copolymer proton-exchange membranes cross-linked with DIPB, *J. Membr. Sci.* **2011**, *383*, 50-59.

40. Teubner, M.; Strey, R. Origin of the scattering peak in microemulsions, *J. Chem. Phys.* **1987**, *87*, 3195-3200.
41. Kinning, D. J.; Thomas, E. L., Hard-sphere interactions between spherical domains in diblock copolymer, *Macromolecules* **1984**, *17*, 1712− 1718.
42. Smit, I.; Bezjak, A. Structural changes in the grafted copolymer polyethylene-styrene, *Polymer* **1981**, *22*, 590-596.
43. Percus, J. K.; Yevich, G. J. Analysis of classical statistical mechanics by means of collective coordinates, *Phys. Rev.* **1958**, *110*, 1-13.
44. Izawa, K.; Ogasawara, T.; Masuda, H.; Okabayashi, H.; Monkenbusch, M.; O'Connor, C. J. Growth process for fractal polymer aggregates formed by perfluorooctyltriethoxysilane. Time-resolved small-angle X-ray scattering spectra and the application of the unified equation, *Colloid Polym Sci* **2002**, *280*, 725–735.
45. Beaucage, G. Small-Angle Scattering from Polymeric Mass Fractals of Arbitrary Mass-Fractal Dimension, *J. Appl. Crystallogr.* **1996**, *29*, 134-146.
46. Beaucage, G.; Schaefer, D. W. Structural studies of complex systems using small-angle scattering: a unified Guinier/power-law approach, *J. Non-Cryst. Solids* **1994**, *172–174*, 797-805.
47. Ashfag, A.; Clochard, M.-C.; Coqueret, X.; Dispenza, C.; Driscoll, M. S.; Ulanski, P.; Al-Sheikhly, M. Polymerization reactions and modifications of polymers by ionizing radiation, *Polymers* **2020**, *12*, 2877.
48. Flory, P. J. Statistical mechanics of swelling of network structures, *J. Chem. Phys.* **1950**, *18*, 108-111.

49. Motegi, T.; Yoshimura, K.; Zhao, Y.; Hiroki, A.; Maekawa, Y. Direct Observation and Semiquantitative Analysis of Hierarchical Structures in Graft-type Polymer Electrolyte Membranes using AFM Technique, *Langmuir* **2022**, *38*, 9992-9999.